Applied Thermal Engineering 199 (2021) 117507

Contents lists available at ScienceDirect

Applied Thermal Engineering

journal homepage: www.elsevier.com/locate/apthermeng

Experimental characterisation of a cold thermal energy storage unit with a pillow-plate heat exchanger design

Håkon Selvnes *, Yosr Allouche, Armin Hafner

Norwegian University of Science and Technology, Department of Energy and Process Engineering, Kolbjørn Hejes vei 1B, NO-7491 Trondheim, Norway

ARTICLE INFO

Keywords:
Cold thermal energy storage
Phase change materials
CO_2 refrigeration
Industrial refrigeration

ABSTRACT

Cold Thermal Energy Storage (CTES) technology can be introduced to refrigeration systems for air conditioning and process cooling to reduce the peak power consumption by decoupling the supply and demand of refrigeration. In these systems, the refrigeration demand can vary significantly over a day, resulting in a challenging peak and valley load pattern on the electrical grid. This paper presents the design, development, and experimental performance investigations of a novel plates-in-tank CTES unit design intended for integration into pump-circulated CO_2 industrial refrigeration systems. The CTES unit is composed of a stainless steel container filled with water as the latent storage medium and fitted with a pillow plate heat exchanger. The refrigerant (CO_2) circulates within the heat exchanger to transfer heat with the storage medium. The current study demonstrates the feasibility of implementing a latent CTES unit directly into the primary refrigerant circuit for peak shaving of the refrigeration load. The results show that the evaporation and condensation temperatures of the refrigerant are the most critical parameters influencing the performance of the charging and discharging cycles, respectively. The unit demonstrated a mean discharge rate of 7.90 kW over a total discharging cycle time of approximately 4.5 h. The resulting maximum discharged energy was calculated to 35.29 kWh.

1. Introduction

The demand for electricity in modern society is high. The peak and valley consumption pattern that is dominating today is a challenge for the grid. Also, the demand pattern is becoming more distinct due to the decarbonisation of industry, transport and the building sector [1–4]. The energy demand for space cooling in the building sector has more than tripled since 1990, making space cooling the fastest-growing end-use in buildings [5]. Furthermore, space cooling for residential and commercial buildings is expected to contribute significantly to the increase in peak power demand towards 2050 [6]. With the current growth in the air-conditioning market, the IEA predicts that over 40% of the total peak power demand in hot climates will be caused by space cooling in 2050 [6]. Consequently, there is undoubtedly a need to introduce new technologies that can reduce the peak load on the electrical grid. Thermal Energy Storage (TES) can represent one solution, as it allows for peak shaving of the thermal demand, ranging from several cycles per day to a seasonal timescale depending on the application [7]. A term often used to designate TES systems operating at sub-ambient temperatures is Cold Thermal Energy Storage (CTES). CTES integrated into Air-Conditioning (AC) systems for buildings have shown good performance by enabling peak shifting of up to 100% of the cooling load to off-peak hours depending on system design [8]. This approach has been particularly popular for commercial buildings occupied only during working hours, which causes a substantial difference in the peak and off-peak cooling load [9]. TES systems employing the sensible heat storage principle is considered mature technology. Commonly used storage materials for sensible heat storage are chilled/hot water, glycol mixtures, rock and concrete. However, the main limitation of these materials is their limited storage capacity over the operating temperature range of the systems in which they are integrated. Chilled water systems for AC commonly use a 7 °C supply temperature and 12 °C return temperature, resulting in a high volume requirement for storing the energy in a chilled water tank. Latent heat storage is considered a developing solution that has demonstrated improved storage performance compared with sensible heat storage solutions. Latent heat storage provides high energy density storage, a tailored phase change temperature and a near-constant storage temperature during the charging and discharging processes [10].

Selvnes et al. [11] proposed a classification of latent CTES with Phase Change Material (PCM) applied to refrigeration systems into two categories; CTES units integrated into the primary refrigerant circuit and

* Corresponding author.
E-mail address: hakon.selvnes@ntnu.no (H. Selvnes).

https://doi.org/10.1016/j.applthermaleng.2021.117507
Received 7 May 2021; Received in revised form 22 July 2021; Accepted 26 August 2021
Available online 3 September 2021
1359-4311/© 2021 The Author(s). Published by Elsevier Ltd. This is an open access article under the CC BY license (http://creativecommons.org/licenses/by/4.0/).

Nomenclature

Abbreviations

COP	Coefficient Of Performance
CTES	Cold Thermal Energy Storage
HEX	Heat Exchanger
HTF	Heat Transfer Fluid
P&ID	Piping and Instrumentation Diagram
PCM	Phase Change Material
PP	Pillow Plate
PWM	Pulse-Width Modulation
TES	Thermal Energy Storage
ACC	Auxiliary CO_2 Circuit
GHC	Glycol Heating Circuit
PCC	Primary CO_2 Circuit
SCC	Secondary CO_2 Circuit

Symbols

$\dot{E}$	energy flow [kW]
$\dot{m}$	mass flow rate [kg/s]
b	thickness [m]
d	diameter [m]
E	energy [kWh]
h	enthalpy [kJ/kg]
L	length [m]
n	number [–]
s	welding spot pitch [m]
T	temperature [K]
t	time [s]
W	width [m]

Greek letters

δ	height [m]
ρ	density [kg/m^3]

Subscripts

CO_2	carbondioxide
PCM	phase change material
PP	Pillow Plate
SW	Spot Weld
C	charging
D	discharging
fus	fusion
g	glycol
i	inner
in	inlet
L	longitudinal
lat	latent
o	outer
out	outlet
s	solid
sat	saturation
T	transversal
th	theoretical
w	wall

CTES units integrated into the secondary refrigeration circuit. In the first category, the CTES unit is directly integrated into the main refrigeration circuit employing a PCM/two-phase fluid Heat Exchanger (HEX) design. The storage acts as an evaporator during the charging process and operates as a condenser for the refrigeration system during the discharging process. In the second category, the storage is integrated into the secondary refrigerant circuit employing a PCM/single-phase fluid HEX design. A secondary refrigerant circuit is commonly used in larger chiller applications, using chilled water, glycol or brine as the secondary refrigerant. During the charging process, the secondary refrigerant is pumped through the CTES unit, acting as a heat source. During the discharging process, the CTES unit acts as a heat sink for the system. Ice bank CTES systems have commonly been applied to high-capacity chiller systems for process cooling purposes, particularly in the dairy industry [12]. During the charging process, ice is formed gradually around the surface of the tubes in which the cold heat transfer fluid (glycol/brine) circulates. The most investigated configurations for CTES units integrated into the secondary refrigerant circuit are the tube-in-tank [13–18] and coil-in-tank designs [19–25], probably due to a relatively simple design and low cost. Despite the higher heat transfer characteristics, CTES units based on the plates-in-tank design are less frequently studied, probably due to the limited availability of plate designs suitable for this application. Furthermore, the higher cost and the lower feasibility of creating a suitable lab-scale test facility based on the plate-in-tank design are possible causes. Only a few recent studies investigating the novel plates-in-tank design were found in the literature and only for positive temperature applications [26,27].

The chiller energy efficiency is positively influenced by the direct integration of a CTES unit into the primary refrigeration circuit compared to a secondary refrigerant circuit because the evaporation temperature of the refrigeration system can be increased during the charging process [28]. Since the evaporation temperature of the refrigeration system is lifted, the pressure lift of the compressors is reduced. This configuration is still not thoroughly described in the literature but has received increased attention, especially over the last five years. The integration of a shell-and-tube PCM-HEX into a 5 kW air-to-air AC unit was experimentally and numerically investigated by Wang et al. [29–31]. The results have shown that integrating the PCM-HEX as a subcooler downstream the condenser could increase the Coefficient Of Performance (COP) by 8% in UK climate conditions. Korth et al. [28] suggested using a tube-in-tank PCM-HEX CTES design integrated into a multi-split AC system to reduce the load on the compressor in the system during peak hours. The experimental results have demonstrated that the PCM-HEX could achieve a mean discharge rate of 1.5 kW for 2.33 h. Furthermore, Korth et al. [32] carried out theoretical modelling and experimental tests on the same tube-in-tank PCM-HEX integrated as a subcooler downstream of the condenser in a 6 kW AC system. The paraffin Parafol 16–97 [33] was used as the PCM, which has a melting point of 18 °C. The experimental results have shown an increase in the evaporation capacity of the AC system by 18% when using the storage for a condensing temperature of 35 °C.

A novel type of HEX that has gained increased attention in industrial applications is the Pillow Plates (PP) HEX. Besides the high heat transfer exchange rate, the application of PP-HEX is interesting as it can be used as an immersed HEX in systems with high operating pressure on the inner flow channel (>80 bar) due to its fully welded design of each single PP. PP-HEX are therefore suitable for integration into the primary refrigerant circuit. The PPs can be manufactured to withstand operating pressures up to 120 bar, and the PP-HEX design is then appropriate for transcritical CO_2 refrigeration systems. Compared to conventional HEX types (e.g. shell and tube), the PP-HEX is a relatively young technology. The main limitations of the PP-HEX to date are the higher cost compared to conventional HEX and limited suppliers of these products. One PP is represented in Fig. 1a. It consists of two thin metal sheets spot-welded together in a particular repetitive pattern by a laser-welding machine. The spots form a defined channel where the refrigerant flows and exchange heat with the storage medium. The two metal plates are also seam-welded along the edges to ensure the sealing of the PP. Two pipes

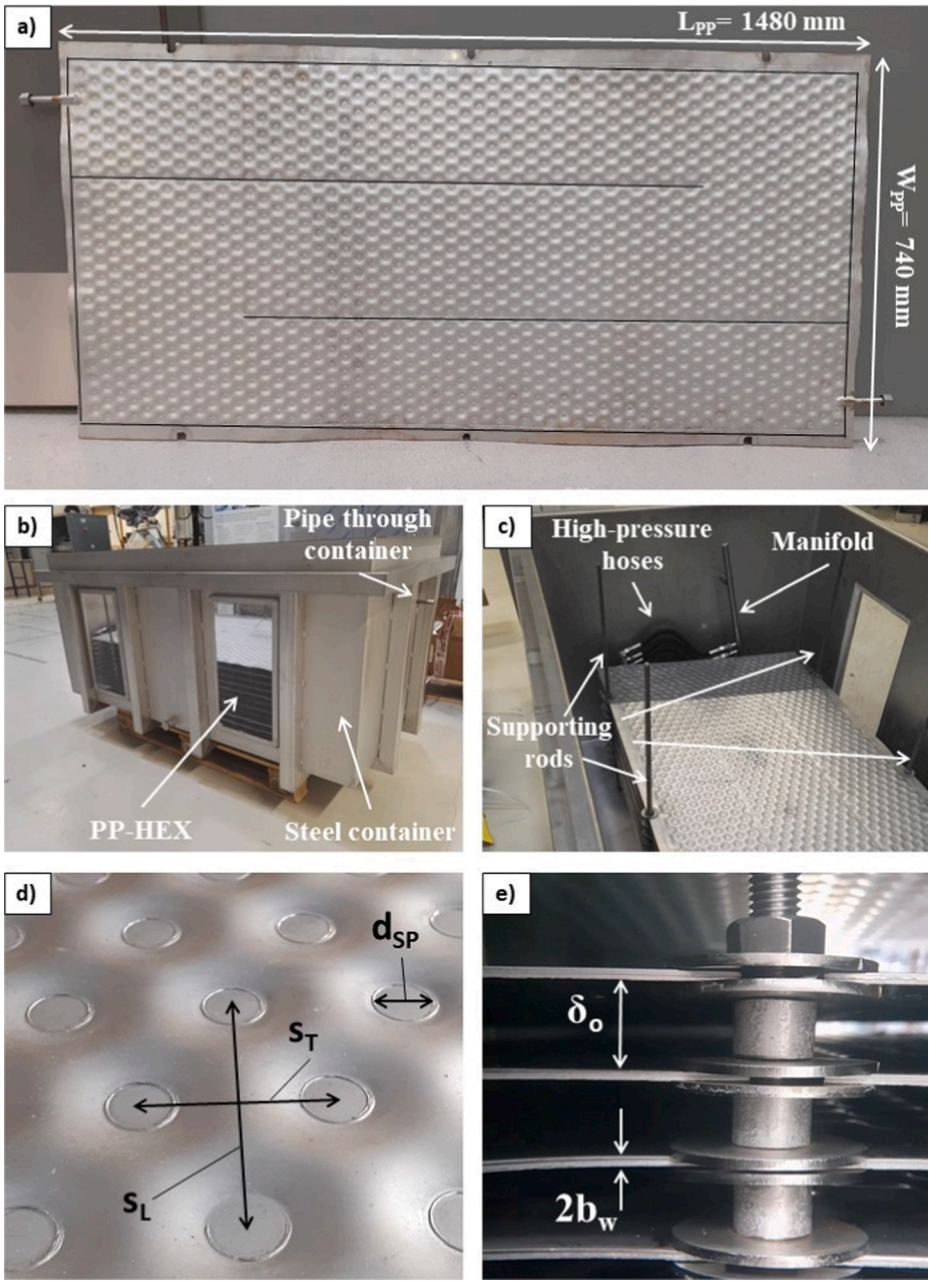

Fig. 1. Overview of the novel CTES unit showing the details of a) one PP for CO_2 refrigeration with inlet/outlet pipes and the seam welds marked with black lines b) the CTES unit before assembly in the test facility c) view of the PP-HEX inside the container d) the wavy PP surface characteristic with the welding pattern parameters e) the PP-HEX stack in the CTES unit with vertical plate pitch.

acting as refrigerant collectors are welded from both sides of the PP, ensuring the inlet and outlet of the refrigerant. After the welding process, the plate is inflated by a hydroforming process, applying high water pressure to the inside of the plate. This process creates the flow channels for the fluid inside the PP and its main wavy surface characteristic (see Fig. 1d). Any number of PP can then be stacked vertically or horizontally, forming a complete PP-HEX.

Although PP-HEX is an emerging design used in chemical and process applications, the published literature on design methods, heat transfer calculation and flow patterns in this type of HEXs remain limited. The mathematical description of the surface and the flow channel cross-section is more challenging than for conventional HEX due to the complex channel shape created by the hydroforming process and its periodicity. Until the date, the published literature on PP-HEX covers both experimental [34–36] and numerical investigations [37–42]. Most studies on PP-HEX use a configuration with a cold and hot stream pair; one stream flowing inside the PP channel and the other stream flowing over the external surface of the PP. Mitrovic and Peterson [34] performed an experimental study of a PP-HEX applied as a condenser for the process fluid located at the top of a distillation column. The experiments were carried out with Marlotherm oil (single-phase) and isopropanol (two-phase) as the hot stream flowing between the PPs, and cooling water as the cold stream flowing inside the PPs. The correlations for the heat transfer and the pressure drop occurring between the condensing isopropanol and the cooling water were developed. However, the application was limited to the specific HEX geometry and the fluid used in the study. Mitrovic and Maltic [37] numerically investigated the effect of the flow parameters and channel geometry on the thermo-hydraulic performance of PPs. It was shown that using a PP provides a heat transfer improvement up to four times compared to a flat

channel with plane walls. However, the PP generally generated a higher pressure drop than the corresponding flat channel geometry. Piper et al. [43] performed a numerical study of PP using forming simulations in the Finite-Element-Analysis software ABAQUS. The study aimed to establish a method of determining the hydraulic diameter, cross-sectional area and heat transfer area of PPs. The results show that the forming simulation could reproduce the PP surface shape with a deviation of less than 4%, and expressions for the design parameters of PP were provided based on the results. Tran et al. [35] carried out experimental investigations on both a lab-scale and a pilot-scale PP-HEX applied as condensers in distillation columns. In the pilot-scale PP-HEX, condensation of chlorobenzene occurred between the PP by flowing cooling water inside the PP. Piper et al. [38] numerically investigated the heat transfer and fluid dynamics in a periodic element of a PP for single-phase turbulent flow (water). The investigation showed that two distinct zones characterise the flow; the meandering core and the recirculating zone forming in the wake of the welding spots. The parametric study has revealed that a longitudinal welding pattern, a larger inflation height and a low Reynolds number generates the highest HEX efficiency (heat transfer to pressure loss ratio). Additionally, the results showed that using oval welding spots increased the HEX efficiency up to 37% compared to the conventional round type. For oval spot welds, the size of the recirculating zone was reduced, which was the main contributor to the pressure loss in the PP. In further work, Piper et al. [39] proposed different models to describe the heat transfer and pressure loss for single-phase turbulent forced convection flow in PPs. The equations were fitted with validated CFD data obtained in [38], achieving a relative deviation of less than 6% for the pressure loss and less than 15% for the heat transfer compared to the numerical data. To the authors best knowledge, only one study can be found in the literature on the two-phase heat transfer characterisation inside the PP channel. The evaporation of the refrigerant R134a was experimentally investigated inside a PP in both natural and forced circulation operations modes [36]. The two-phase heat transfer coefficient for the evaporation process inside the PP channel was determined. A numerical investigation on the influence of various geometrical parameters and flow conditions on the PP performance was performed by Shirzad et al. [41]. The results agreed with those obtained by Piper et al. [38], and here it was shown that a PP with a larger inflation height (from 3 mm to 7.5 mm) improves the HEX performance by up to 4 times due to a reduction in the pressure loss (Reynolds number of 1000). Additionally, increasing the longitudinal spot weld distance from 53 mm to 73 mm improved the efficiency by 5% at a Reynolds number of 6000. A similar study was performed by Kumar et al. [42], where increasing the PP channel height from 3 mm to 6 mm resulted in a decrease in specific pressure drop of 81% and an increase in the Nusselt number of 29%. Overall, this improved the HEX efficiency by a factor of 3. The results have also revealed that increasing the welding spot diameter have a negligible effect on the heat transfer in the channel. However, the pressure loss was found to be higher with larger welding spots. Consequently, the overall HEX efficiency was reduced. Arsenyeva et al. [40] established a method for the design of PP-HEX based on predefined process conditions of the cold and hot streams in addition to limits of pressure loss and heat transfer in the HEX. The proposed method evaluates the overall heat transfer coefficient and velocities in both the external channel (between each PP) and inner channels for several PP geometries. By fully exploiting the allowable pressure drop of the cold stream in the inner PP channel, the distance between each PP was varied to find the minimum heat transfer surface area that satisfies the operating conditions. The results show that the PP-HEX requires approximately 30% lower heat transfer area compared to a chevron type plate HEX when using water as both the hot and cold streams.

Natural refrigerants such as CO_2, ammonia and hydrocarbons are the most sustainable and environmentally friendly refrigerants [44,45]. CO_2 transcritical refrigeration systems have become the industry standard in supermarket refrigeration for cold and mild climates [46]. Furthermore, CO_2 is becoming a viable alternative in the industrial refrigeration sector with available system capacities in the range of 2–3 MW [47]. Other demonstrated and well-proven CO_2 refrigeration applications are residential water heaters [48] and systems for ice rinks [49]. Demonstration of the performance of HEX units for latent CTES is vital to increase the confidence in this technology by manufacturers and stakeholders in the refrigeration industry. Thorough experimental characterisation of promising PCM-HEX units at a laboratory scale is a measure that can contribute to establishing up-scaled pilot plants and demonstration sites in the refrigeration industry, increasing the market penetration of CTES technology. The design of a novel latent CTES unit based on the PP-HEX design intended as a peak shaving device was first presented by Selvnes et al. [50]. The unit could be integrated into the primary refrigeration circuit of an industrial size CO_2 refrigeration system. The CTES unit, experimental facility, and implementation strategy were described in detail. The initial results using water as the storage medium were then presented by Selvnes et al. [51]. In the current paper, the performance of the novel PP CTES unit is tested for various PP configurations and refrigerant parameters using water/ice as the PCM. During the charging process, heat is transferred from the PCM to the CO_2 so that the storage medium solidifies and the refrigerant evaporates. During the discharging cycle, heat is transferred from the CO_2 to the PCM so that the storage medium melts and the refrigerant condenses. First, a presentation of the CTES unit and the experimental setup is given, followed by a description of the experimental procedure for the charging and discharging cycles. Finally, the results from the experimental characterisation of the CTES unit are presented and discussed separately for the charging and discharging processes.

2. Experimental setup

2.1. Cold thermal energy storage unit

The novel CTES unit is shown in Fig. 1b. It is composed of a plates-in-tank HEX design immersed in water as the cold storage medium for industrial refrigeration applications (see Fig. 1c). Using water as the cold storage medium is suitable for peak shaving of the cooling load in refrigeration systems for AC or process cooling in the temperature range of 0 °C to 10 °C. Heat is transferred to/from the flowing refrigerant in the PP during the storage charging/discharging processes, respectively. The plates-in-tank design consists of a stack of ten PP constructed of stainless steel. The main design parameters for the PP-HEX are the overall PP length (L_{PP}), the width (W_{PP}), the maximum vertical distance between each PP (δ_o) and the number of plates (n_{PP}). One PP is represented in Fig. 1a. It is composed of two metal sheets of stainless steel with a thickness of 1 mm welded together by a laser-welding machine.

The main geometrical design parameters of one PP are the following (see Fig. 1d-e): the spot weld diameter (d_{SW}), the transversal spot weld pitch (s_T), the longitudinal spot weld pitch (s_L), the channel maximum inflation height (δ_i) and the PP wall thickness (b_w). In this study, a longitudinal welding spot pattern was applied to the PP. It has a longitudinal welding spot pitch of 50 mm and a transversal welding spot pitch of 30 mm. This parameter selection results in a triangular configuration commonly found in the PP industry. The detailed view of the PP surface in Fig. 1d clearly shows the staggered spot-weld pattern of the PP, which promotes the mixing of the flow as well as an improving heat transfer between the refrigerant and the storage medium [38]. Two longitudinal seam welds are performed on the plate, as indicated in Fig. 1a. It generates three flow passes for the refrigerant to flow between the inlet and outlet pipe. This technique is used to direct the refrigerant flow and ensure a better distribution through the channels to maximise the heat exchange between both mediums. The plate stack is mounted on a support frame of square steel tube for convenient installation and removal of the stack into the container. The PPs are fixed in the frame by six metal supporting rods, three along each side of the plates (see Fig. 1c). The distance (pitch) between the PPs in the PP-HEX can be varied using different lengths of cylindrical spacers and washers on the

metal rods, shown in Fig. 1e. The plate pitch is a key parameter for the proper design of the CTES unit. The selection of the PP pitch is based on the thermal properties of the PCM, the required storage capacity and the refrigeration load profile of the process. In the current investigation, the experimental performance characterisation of the CTES unit is carried out with three vertical plate-to-plate pitches (δ_o): 15 mm, 30 mm, and 45 mm. The same number of PPs (10) in the stack was used for all the tests. The total heat exchange area for all test campaigns was 21.90 m^2. The inlet and outlet pipe to/from each PP is connected to a manifold by a high-pressure braided hose at their respective ends of the PP-HEX (see Fig. 1c). The CTES unit is connected to the experimental test facility by a pipe from the manifold that passes through the container wall, shown in Fig. 1b. The stack of PP is placed into a stainless-steel container which is supported by a frame of square steel tube. The PCM is filled into the container so that the PP-HEX is completely immersed in liquid. A lid is placed at the top of the container to prevent the evaporation of the PCM. The CTES unit is equipped with two windows of thick acrylic plexiglass on each side for visual observation of the melting and freezing process of the PCM as shown in Fig. 1b. The container is insulated using 50 mm polystyrene plates. The container is fitted with a service valve to drain the PCM when needed. The main geometrical parameters of the CTES unit are summarised in Table 1.

2.2. Experimental test facility

An experimental test facility is designed by the authors and constructed to test the performance of the CTES unit [50]. A simplified Piping and Instrumentation Diagram (P&ID) of the test facility is shown in Fig. 2. The purpose of the facility is to set and monitor the thermo-hydraulic conditions of the refrigerant at the inlet of the CTES unit during the charging and discharging processes. The facility is operated in two different modes: Charging mode (indicated with green lines in Fig. 2) and discharging mode (indicated with purple lines in Fig. 2). Four circuits can be identified in the facility: The Primary CO_2 Circuit (PCC), the Secondary CO_2 Circuit (SCC), the Glycol Heating Circuit (GHC), and the Auxiliary CO_2 Circuit (ACC). During the charging mode, the PCC and the ACC are in operation. When the facility is operating in discharging mode, the SCC and the GHC are active. The total charge of refrigerant in the PCC/SCC is approximately 50 kg.

The location of sensors for mass flow rate, temperature, pressure and differential pressure are indicated in Fig. 2. The pressure of the PCC/SCC is measured by an absolute pressure transmitter (P1) calibrated in the pressure range 0–70 bar. Three differential pressure transmitters calibrated in the pressure range 0.03–3 bar are installed to measure the pressure drop across the evaporator HEX (DP1), the CTES unit (DP2) and the condenser HEX (DP3). The refrigerant temperature through both the charging and discharging processes in the PCC/SCC is measured by five RTD Pt100 temperature sensors as follows: inlet and outlet of the CTES unit (T1 and T2), outlet of condenser HEX (T3), outlet of CO_2 pump (T4) and outlet of the evaporator (T5). The water temperature in the CTES unit is measured by T-type thermocouples (TC) located on the top surface of the PPs. A top view of one PP showing the main geometrical characteristics and position of the thermocouples is represented in Fig. 3. Three PPs are selected according to their height in the plate stack. Each of these PPs is equipped with nine consecutively numbered thermocouples distributed on its surface as follows: The thermocouples TC00-TC08 are mounted on PP 2, TC09-TC17 are mounted on PP 5 and TC18-TC26 are mounted on PP 9. The control of the test facility and the collection of the measurement data are achieved using a data acquisition system coupled with LabView software [52]. An overview of the measurement equipment is given in Table 2.

Table 1
Main geometrical parameters of the novel CTES unit.

Parameter	Value
s_L	50 mm
s_T	30 mm
d_{SW}	10 mm
δ_i	4.3 mm
b_w	1.0 mm
L_{PP}	1480 mm
W_{PP}	740 mm
δ_o	15/30/45 mm
n_{PP}	10

The charging process is carried out through the PCC. All CO_2 tubing is K65 copper tubes with brazed joints, while all service valves (V1-V4) are manual ball valves (Refrigera Industriale [53]). The circulation of the refrigerant is assured by a hermetic centrifugal refrigerant pump (CO_2 pump) that is fitted with an inverter for frequency control to control the refrigerant flow rates (CAMh 2/4, AGX3.0 PN60, Hermetic Pumpen GmbH [54]). From the outlet of the CO_2 pump, the refrigerant flow is separated into two pipes: A recirculation pipe back to the receiver and a pipe going to the CTES unit. The recirculation pipe is included according to the specification of the pump manufacturer to assure the minimum flow requirement of the CO_2 pump. A Coriolis flowmeter (FT2) is used to measure the inlet CO_2 mass flow rate to the CTES unit. The refrigerant enters the CTES at a liquid state through valve 2 (V2). The refrigerant evaporates as it flows through the CTES unit as heat is transferred from the storage medium to the refrigerant. At the outlet of the CTES, the refrigerant is a mixture of liquid and vapour. The CO_2 mixture is then circulated through the condenser plate HEX (CBXP52, Alfa Laval), which is connected to the ACC to condense the refrigerant in the PCC to the liquid state. From the outlet of the condenser, the liquid CO_2 is circulated to the refrigerant receiver. Then the liquid is drawn from the bottom of the receiver, and the cycle continues until the charging process is completely achieved.

The ACC has a double function. First, it provides the cooling of the PCC during the charging process. The cooling is achieved by supplying liquid refrigerant through an electronic expansion valve (EEV 1, CCMT-2, Danfoss). Second, it also maintains the desired pressure in the PCC during standstill by supplying cooling in the subcooler through EEV 2 (AKVH 10-3, Danfoss). Both valves are operated by fully automatic Danfoss superheat controllers (EKD 316C and AK-CC550A, respectively). The ACC is connected to the liquid line and suction lines of a CO_2 booster refrigeration system in the laboratory to accomplish these two functions. This refrigeration system has three evaporation levels (−10 °C, −30 °C and −50 °C) that can be chosen by operating a valve station (see Fig. 2). A stepper-type valve (V5, CCMT42, Danfoss) is fitted in the suction side of the ACC. This valve is operating as a back pressure valve to manually control the evaporation pressure of the ACC if an evaporation pressure between the fixed levels is required. By decreasing the evaporation pressure of the ACC, the pressure of the PCC will also decrease. Consequently, experiments with a wider range of evaporation temperatures in the PCC can be carried out.

The discharging process is carried out through the SCC, which is connected to a GHC to simulate the thermal load. Liquid CO_2 is drawn from the bottom of the receiver by the CO_2 pump and circulated to the evaporator plate HEX (CBXP112, Alfa Laval) through valve 1 (V1). In the evaporator, heat is transferred from the glycol to the refrigerant so that the CO_2 exits the evaporator as a liquid/vapour mixture. The two-phase CO_2 then circulates through the CTES unit, where heat is transferred to the storage medium and the refrigerant condenses to a fully liquid state. The liquid then returns to the refrigerant receiver through valve 3 (V3), completing the cycle. The Heat Transfer Fluid (HTF) in the GHC consists of a mixture of 30% propylene glycol and water (DowCal 200, [55]). The glycol is supplied to the evaporator by a circulation pump (UPS25-125, Grundfos). The glycol mass flow rate is measured by a Coriolis mass flow meter (FT 1). The heat input to the GHC is achieved by two 9 kW electric immersion heaters. One of the heaters is fitted with pulse-width modulation (PWM) control for precise regulation of the

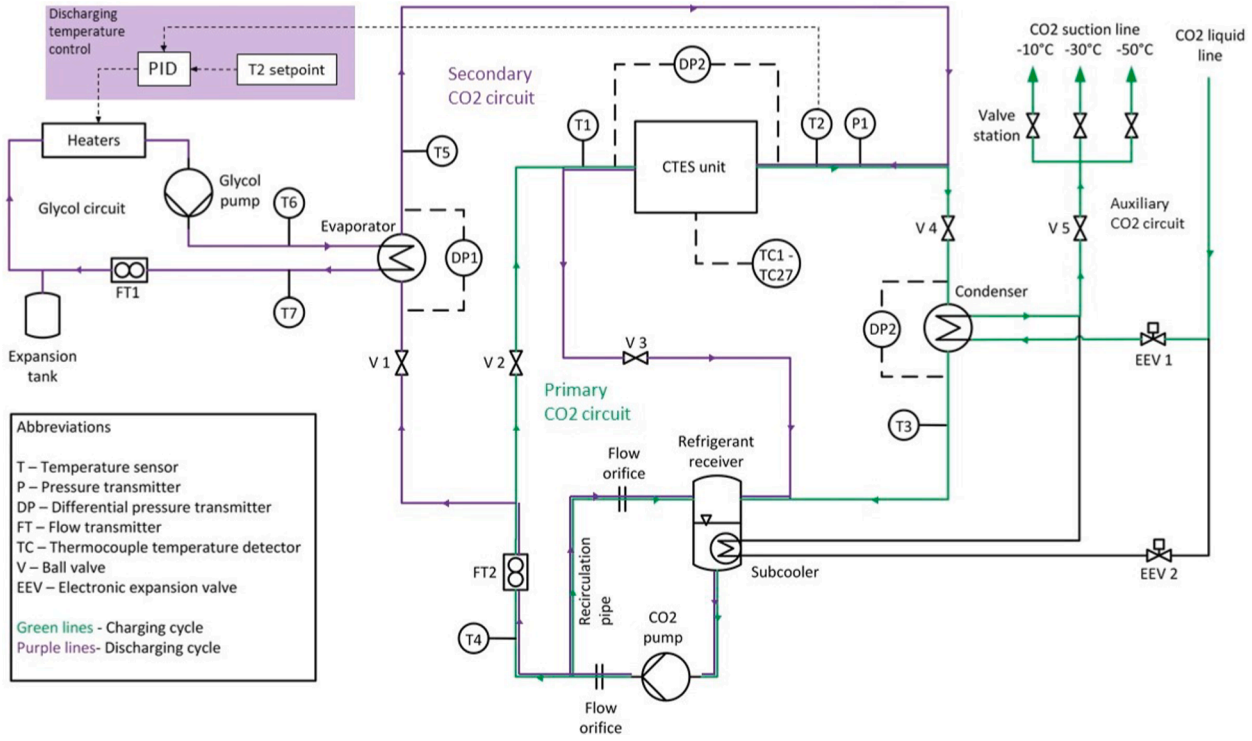

Fig. 2. Piping and instrumentation diagram (P&ID) of the test facility.

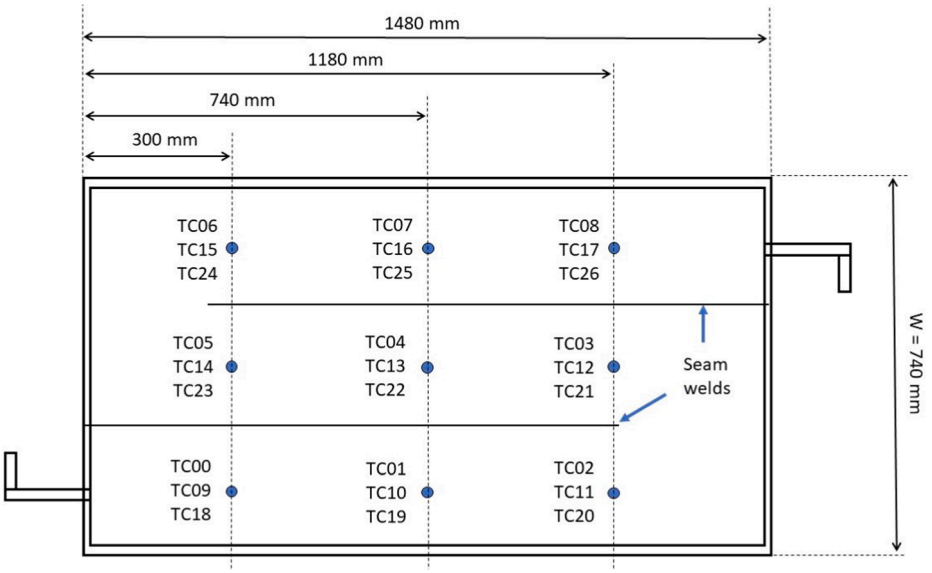

Fig. 3. Top view of a PP: Locations of thermocouples on three selected PPs.

power output from 0 to 100%. Furthermore, two RTD Pt100 temperature sensors are mounted in the inlet (T6) and outlet (T7) pipe of the evaporator to measure the inlet and outlet temperature of the glycol, respectively.

3. Experimental procedure

3.1. Charging process

The charging process consists of extracting heat from the PCM storage medium to the refrigerant. Consequently, the PCM solidifies (heat release) and the refrigerant evaporates (heat absorption). During the charging process (see Fig. 2), valve 1 (V1) and valve 3 (V3) is closed so that the CO_2 refrigerant circulates through the PCC as described in Section 2.2. In this study, a series of experiments considering various refrigerant mass flow rates and evaporation temperatures were conducted for each plate pitch. The refrigerant evaporation temperature was varied from −2.5 °C to −15 °C, and the mass flow rate was varied from 4 kg/min to 10 kg/min. The charging process in each test was run until completion to compare storage capacities and charging time of the different HEX configurations and operating conditions. The charging process starts when the average value given by the first placed TC on each plate is measured below 5 °C. TC00, TC09 and TC17 are the closest sensors to the refrigerant inlet on PP2, PP5 and PP9, respectively. As the

Table 2
Measurement equipment utilised in the test facility.

Component	Model	Producer	Indicated accuracy
Absolute pressure transmitter	Cerabar S PMP71	Endress+Hauser	±0.25% of set span
Differential pressure transmitter	Deltabar S PMD75	Endress+Hauser	±0.15% of set span
Temperature sensor CO_2 and glycol	Class B RTD Pt100	RS PRO	±0.1 K
Temperature sensor water	Thermocouple type T	RS PRO	±0.2 K
Mass flow meter glycol	RHM 15 Coriolis meter	Rheonik	±0.2% of reading
Mass flow meter CO_2	RHM 06 Coriolis meter	Rheonik	±0.2% of reading

charging process takes place, an ice layer on each plate is formed and becomes thicker as the charging process progresses. The charging process ends when an ice block is formed between two adjacent PPs, i.e. when the ice layer on the two PPs has overlapped. At this point, energy storage is carried out through a sensible energy storage process until the temperature of the ice block approaches the inlet refrigerant temperature. In the tests, the end of the charging cycle is that corresponding to a temperature difference between the mean value of the last-placed TC on each instrumented PP (TC8, TC17 and TC26) and the refrigerant saturation temperature, is lower than 0.2 K. This period from the first temperature sensors (TC00, TC09 and TC17) measures a storage medium temperature below 5 °C and the last temperature sensors (TC8, TC17 and TC26) approaches the refrigerant evaporation temperature by 0.2 K is defined as the charging time. The progress of the charging cycle can also be easily observed by following the ice block thickness through the four windows on the CTES unit (see Fig. 1b). The theoretical maximum latent storage capacity of the CTES unit depends on the PP size and the vertical plate-to-plate pitch. Due to the pillow-like surface of the plates, the vertical distance between two plates varies across the surface. The mean vertical plate-to-plate pitch $\delta_{o,mean}$ is approximated as the mean value between the maximum (δ_o) and the minimum (δ_o - δ_i) distance between two adjacent plates, as given by Eq. 1:

$$\delta_{o,mean} = \frac{1}{2}\cdot((\delta_o - \delta_i) + \delta_o). \quad (1)$$

The maximum theoretical latent storage capacity is calculated considering only the PCM volume between the PPs as the active PCM volume. Furthermore, it is assumed that the ice layer below PP1 and above PP10 has grown to a thickness of half the vertical plate pitch when the charging cycle is complete (see Fig. 1e). The theoretical maximum latent storage capacity can be calculated as follows:

$$E_{lat,th} = h_{fus,\mathrm{PCM}}\cdot\rho_{s,\mathrm{PCM}}\cdot(W_{\mathrm{PP}}\cdot L_{\mathrm{PP}}\cdot\delta_{o,mean}\cdot n_{\mathrm{PP}}) \quad (2)$$

where $E_{lat,th}$ is the theoretical maximum latent storage capacity of the CTES unit, $h_{fus,\mathrm{PCM}}$ is the specific enthalpy of fusion of the PCM, and $\rho_{s,\mathrm{PCM}}$ is the solid density of the PCM. The last term of Eq. 2 ($W_{\mathrm{PP}}\cdot L_{\mathrm{PP}}\cdot\delta_{o,mean}\cdot n_{\mathrm{PP}}$) is the total active volume of PCM in the CTES unit. The mass flow rate of the CO_2 in the PCC is adjusted by controlling the frequency output of the inverter for the CO_2 pump in the range 35–50 Hz. If a lower mass flow rate is required than the minimum frequency, the flow is throttled by partly closing valve 2 (V2, see Fig. 2). The evaporation temperature of the CO_2 in the CTES unit is set by adjusting the cooling rate of the ACC in the condenser. The pressure in the primary CO_2 is kept constant as the same extracted heat rate from the CTES unit is rejected through the condenser. When a higher cooling rate is provided to the condenser, the pressure of the PCC is lowered.

3.2. Discharging process

The discharging process consists of the heat transfer from the refrigerant to the storage medium. As the refrigerant flows inside the PPs, heat is rejected to the storage medium until the refrigerant is completely condensed at the outlet of the PP manifold. Consequently, the PCM temperature increases until it is completely melted. During the discharging process, valve 2 (V2) and valve 4 (V4) are closed (see Fig. 2) so that the SCC is active. The flow direction through the CTES unit is reversed compared to the charging cycle so that the inlet and outlet are swapped. The refrigerant mass flow rate is controlled in the same manner as described in Section 3.1. The heat input to the CO_2 from the GHC controls the pressure in the SCC during the discharging cycle. If the heat transferred to the CO_2 in the evaporator equals the heat rejected to the storage medium in the CTES unit, the pressure in the SCC remains constant. In this case, the pressure can be controlled by supplying more or less heat to the secondary circuit. As described in Section 2.2, the output of the electric heaters can be controlled with high precision as one of the heaters is equipped with PWM control. A PI-controller in the LabVIEW software adjusts the output of the PWM-controlled heater from 0% to 100% according to the set point temperature of the refrigerant at the inlet of the CTES unit. Since the discharging cycle is a highly transient process, the PI controller continuously adjusts the heater output to keep the pressure level constant in the secondary circuit. The discharging process continues until all the ice blocks have melted or until the refrigerant is not able to reject any more heat to the CTES unit without increasing the pressure. The discharging time is defined as the period from the start of the discharging cycle until one of these criteria occurs.

For each PP-HEX configuration, a series of experiments considering various CO_2 mass flow rates and condensing temperatures were conducted. The refrigerant condensing temperature was varied from 2.5 °C to 10 °C, and the mass flow rate was varied from 4 kg/min to 10 kg/min. The discharging capacity of the CTES unit is calculated based on the heat flow from the glycol to the CO_2 in the evaporator, assuming there is no heat loss to the ambient. The energy balance for the evaporator is presented in Eq. 3. The thermodynamic properties of the glycol mixture were taken from the data sheet of the manufacturer, assuming a constant specific heat capacity in the relevant temperature range. The refrigerant enters the CTES unit as a two-phase mixture and exits the CTES unit in a subcooled condition. Consequently, the heat transferred from the glycol to the CO_2 in the evaporator is that rejected to the PCM during the discharging process as formulated in Eq. 3 and 4:

$$\dot{E}_{\mathrm{CO_2}} - \dot{E}_g = 0, \quad (3)$$

$$\dot{E}_{\mathrm{CO_2}} = \dot{m}_g\cdot cp_g\cdot(T_{g,out} - T_{g,in}), \quad (4)$$

where $\dot{E}_{\mathrm{CO_2}}$ is the heat flow to the refrigerant in the evaporator, $\dot{E}_g$ is the heat flow from the glycol, $\dot{m}_g$ is the glycol mass flow rate, cp_g is the specific heat capacity of the glycol and $(T_{g,out} - T_{g,in})$ is the temperature difference of the glycol between the inlet and the outlet in the evaporator.

4. Uncertainty analysis and repeatability

The output of the temperature sensors were checked with an ice water bath and validated to operate at within ±0.2 K (thermocouples TC01-TC27, see Fig. 2) and ±0.1 K (RTD100 T1-T7, see Fig. 2) at 0 °C. The uncertainty analysis was carried out by the method elaborated in [56], using a confidence level of 95% (coverage factor of 2). The formulation used for propagation of uncertainty is summarised below. Uncertainty for the mean PCM temperature on PP2, PP5, and PP9 ($T_{PP2,mean}$, $T_{PP5,mean}$, and $T_{PP9,mean}$):

$$u(T_{PCM}) = \sqrt{(1/9)^2 \cdot \sum_{i=1}^{9} u(T_i)}. \quad (5)$$

Uncertainty for the refrigerant saturation temperature:

$$u(T_{CO_2,sat}) = \sqrt{\left(\frac{\partial T_{CO_2,sat}}{\partial P_{CO_2,sat}}\right)^2 \cdot u(P_{CO_2,sat})^2}. \quad (6)$$

From the Antoine equation the relationship between saturation temperature and saturation pressure can be found. By derivation and inserting the coefficients for CO_2, it can be written as:

$$\frac{\partial T_{CO_2,sat}}{\partial P_{CO_2,sat}} = \frac{2273.66}{P_{CO_2,sat} \cdot (17.9834 - \ln(P_{CO_2,sat}))^2}. \quad (7)$$

Uncertainty in the heat flow from the glycol to the refrigerant in the evaporator:

$$u(\dot{E}_{CO_2}) = \sqrt{(cp_g \cdot \Delta T_g \cdot u(\dot{m}_g))^2 + (\dot{m}_g \cdot cp_g \cdot u(\Delta T_g))^2}. \quad (8)$$

Uncertainty in the glycol temperature difference from inlet to outlet in the evaporator:

$$u(\Delta T_g) = \sqrt{u(T_{g,in})^2 + u(T_{g,out})^2}. \quad (9)$$

The uncertainty in the discharged energy over the cycle is estimated by integrating the uncertainty in the heat flow from the glycol (Eq. 8 from the start to the end of the cycle. To investigate the repeatability of the experiments, tests with identical test conditions were carried out for the 30 mm and 45 mm plate pitches. The charging time was used as the indicator for the charging cycle. The resulting range of charging time was found to be <10 min for both the 30 mm and 45 mm plate pitch. This corresponds to a repeatability of the charging time within ±5.9% and ±3.3% at $T_{sat} = -5$ °C and $\dot{m}_{CO_2} = 7$ kg/min for the 30 mm and 45 mm plate pitch, respectively. For the discharging process, the mean discharge rate and discharged energy over the cycle were chosen as indicators for repeatability. The obtained range for the discharged energy over the cycle was <1 kWh for both configurations, corresponding to <5% and <3% of the discharged energy for the 30 mm and 45 mm plate pitch, respectively. For the mean discharge rate, the obtained range was <0.25 kW for both configurations.

5. Results and discussion

5.1. Charging cycle

This section presents the results obtained from the charging tests described in Section 3.1. The mean refrigerant evaporation temperature is calculated using the REFPROP 10 database [57] based on the mean pressure in the CTES unit between the inlet and outlet using transmitter P1 and DP2 (see Fig. 2). The mean pressure drop across the CTES unit during the charging process as a function of the CO_2 evaporation temperature for three mass flow rates ($\dot{m}_{CO_2} = 4$ kg/min, $\dot{m}_{CO_2} = 7$ kg/min and $\dot{m}_{CO_2} = 10$ kg/min) is shown in Fig. 4. The presented values of the pressure drop are the mean value over the complete charging cycle. From Fig. 4 it can be observed that the mean pressure drop increases when the evaporation temperature of the refrigerant is reduced. For a given mass flow rate, as the CO_2 evaporation temperature is reduced, more refrigerant is evaporated in the PP due to the higher temperature difference between the storage medium (water/ice) and the refrigerant. Thus the mean refrigerant density decreases and the mean refrigerant velocity increases, resulting in a higher pressure drop across the CTES unit. An increasing pressure drop difference is observed for the higher refrigerant mass flow rate for the studied evaporation temperature range (-1.5 °C to −10 °C). The pressure drop difference between −1.5 °C and −10 °C was calculated to be approximately 91%, 113% and 138% for $\dot{m}_{CO_2} = 4$ kg/min, $\dot{m}_{CO_2} = 7$ kg/min and $\dot{m}_{CO_2} = 10$ kg/min, respectively.

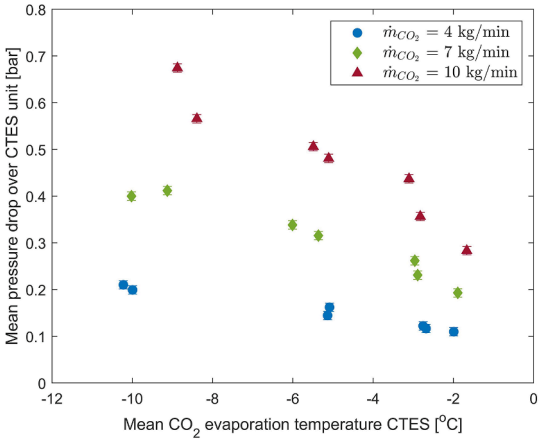

Fig. 4. Mean pressure drop over CTES unit during charging cycle as a function of the refrigerant evaporation temperature for various refrigerant mass flow rates.

The refrigeration capacity of the ACC limited the evaporation temperature to approximately −8.9 °C for the highest refrigerant mass flow rate ($\dot{m}_{CO_2} = 10$ kg/min). Furthermore, increasing the refrigerant mass flow rate increases the mean pressure drop for a given evaporation temperature. At a refrigerant evaporation temperature of −5 °C, the mean pressure drop increases by about 118% and 232% when increasing the refrigerant mass flow rate from 4 kg/min to 7 kg/min and 10 kg/min, respectively. The increase in pressure drop with increasing mass flow rate is caused by an increased mean velocity of the refrigerant in the PP channel.

The mean storage medium temperature adjacent to the PPs in the stack (PP2, PP5 and PP9, see Section 2.2) during the charging process as well as the CO_2 evaporation temperature represented in Fig. 5c using refrigerant mass flow rates of $\dot{m}_{CO_2} = 4$ kg/min, $\dot{m}_{CO_2} = 7$ kg/min and $\dot{m}_{CO_2} = 10$ kg/min, respectively. All three experiments use a plate pitch of 30 mm, an initial temperature of the storage medium of 9 °C and a refrigerant evaporation temperature of −5 °C. For a given refrigerant mass flow rate, as the charging process progresses, the water temperature decreases from the initial temperature to 0 °C (sensible heat storage). When the water temperature reaches 0 °C, the phase change process starts, and the storage medium solidifies. During the phase change process, energy is stored as latent heat, and the charging process progresses with a constant temperature difference between the evaporating refrigerant and the solidifying storage medium. A plateau can then be observed in the temperature profiles to describe the latent heat storage (indicated in Fig. 5a to c). The measured water temperatures on PP2, PP5, and PP9 are approaching the refrigerant evaporation temperature during the latent heat storage period because the thermocouple sensors become embedded in the solid ice layer as the charging progresses. There is a temperature gradient within the solid ice layer in the perpendicular direction of the PP surface, where the temperature ranges from the refrigerant evaporation temperature at the PP surface to the PCM phase change temperature at the liquid-solid interface. After the latent storage period, the storage medium temperature decreases at a higher rate, indicating that the charging process continues as sensible heat storage. The mean storage medium temperature approaches the refrigerant evaporation temperature to denote the end of the charging cycle.

It can be seen from Fig. 5a to c that the experiment time increases for decreasing refrigerant mass flow rates. Compared to a flow rate of $\dot{m}_{CO_2} = 10$ kg/min, the experiment time (from the initial storage temperature to completion) is approximately 8% and 19% longer using a refrigerant mass flow rate of $\dot{m}_{CO_2} = 7$ kg/min and $\dot{m}_{CO_2} = 4$ kg/min, respectively. Furthermore, the storage medium temperature is reduced more rapidly from the initial temperature (9 °C) to the phase change temperature

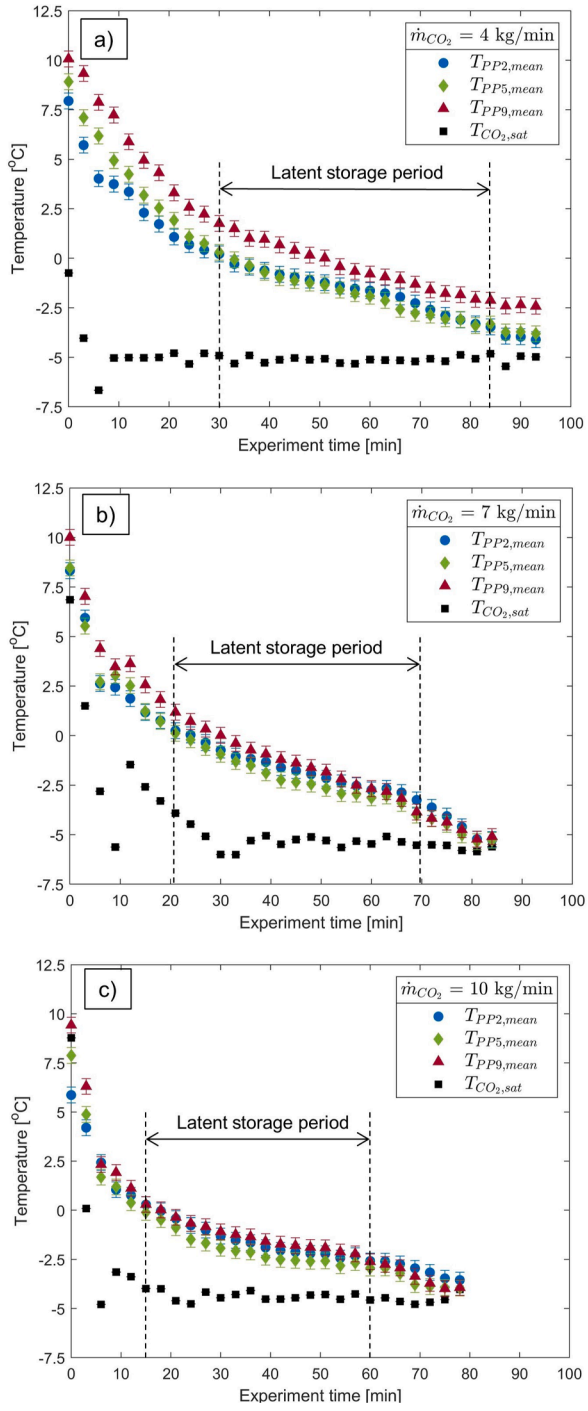

Fig. 5. The mean PCM temperature close to PP 2, 5 and 9 in the stack during the charging cycle with plate pitch δ_o = 30 mm for a refrigerant mass flow rate of a) 4 kg/min b) 7 kg/min and c) 10 kg/min.

using a higher refrigerant mass flow rate. Also, observing the temperature difference through the height of the PP-HEX (T_{PP2}, T_{PP5} and T_{PP9}), a more distinct temperature stratification of the storage medium is observed for the lowest refrigerant mass flow rate (Fig. 5a). These observations are explained by an inadequate refrigerant supply to the PP-HEX to carry out the heat transfer process using the lowest refrigerant mass flow rate. For the flow rate of $\dot{m}_{CO_2}$ = 4 kg/min, it was measured varying degree of superheated refrigerant at the outlet of the PP-HEX during the first 20–30 min of the charging process. This observation means that all refrigerant supplied to the CTES unit has been evaporated inside the PPs before reaching the manifold at the outlet. Superheated refrigerant is generally unwanted, as ensuring a vapour/liquid refrigerant mixture throughout the length of the PPs (flooded condition) ensures the best utilization of the heat transfer area and high heat transfer [58–60]. Furthermore, it was visually observed that the lowest refrigerant mass flow rate resulted in a less uniform ice layer on the PP surface, giving less ice growth at the outer edges of the PPs. Consequently, it can be concluded that a refrigerant mass flow rate of $\dot{m}_{CO_2}$ = 7 kg/min and $\dot{m}_{CO_2}$ = 10 kg/min are more appropriate to produce a uniform ice layer on each PP in the plate stack.

The charging time as a function of the mean refrigerant evaporation temperature and mass flow rates ($\dot{m}_{CO_2}$ = 4 kg/min, $\dot{m}_{CO_2}$ = 7 kg/min, and $\dot{m}_{CO_2}$ = 10 kg/min) for the different configurations are presented in Fig. 6 (δ_o = 15 mm), Fig. 7 (δ_o = 30 mm), and Fig. 8 (δ_o = 45 mm). See Section 3.1 for the definition of the charging time presented here. It can be clearly seen that for all three configurations, the lower the refrigerant evaporation temperature is, the lower the charging time. Indeed, the conduction heat transfer between the PP surface and the solidifying storage medium is the dominant heat transfer mechanism. During the charging process, heat is transferred by conduction from the storage medium to the refrigerant. A solid ice layer is formed on both sides of each PP as the heat transfer progresses. The thickness of the ice layer increases as the charging process is carried out. The charging process ends when a uniform block of ice is developed between each PP. The ice layer growth is the main indicator showing the satisfying progress of the charging process. Nevertheless, the heat transfer will be increasingly limited as the ice layer is developed since it acts as additional thermal resistance to the heat transfer process. One solution to compensate for this phenomenon and decrease the charging time is to increase the temperature difference between the solidifying storage medium and the refrigerant, increasing the driving forces and enhancing the heat transfer. As the phase change temperature of the storage medium is fixed, the temperature difference can only be increased by decreasing the refrigerant evaporation temperature. However, reducing the evaporation temperature increases the required temperature lift of the refrigeration system and directly affects the charging COP. It is established that reducing the evaporation temperature by 1 K will reduce the COP of the refrigeration system by 2–3% [61]. Therefore, it is advisable to operate the system with the highest possible evaporation temperature. However, the optimal evaporation temperature should be selected considering the complete refrigeration system in which the CTES unit is implemented and other factors such as the electricity price and the number of hours available to operate the charging process.

It can also be observed that the charging time is generally reduced by

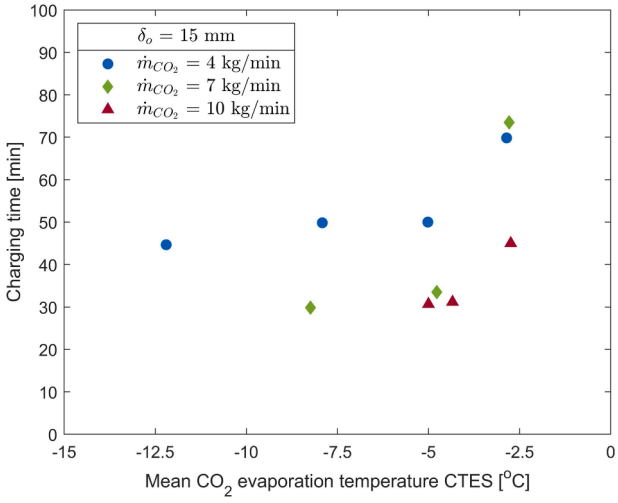

Fig. 6. Charging time for of CTES unit with plate-to-plate pitch of 15 mm as a function of the refrigerant evaporation temperature for various refrigerant mass flow rates.

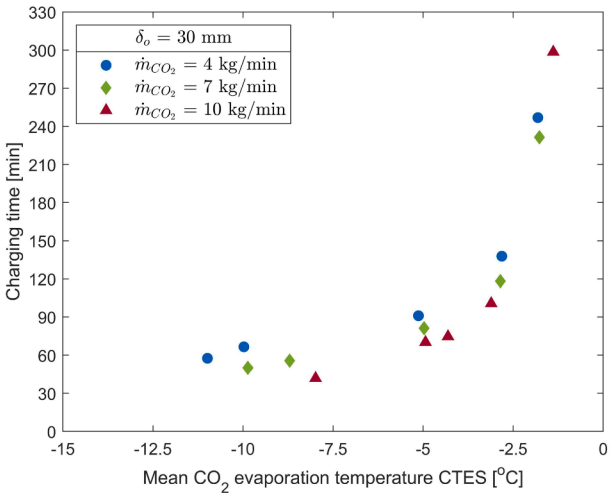

Fig. 7. Charging time for of CTES unit with plate-to-plate pitch of 30 mm as a function of the refrigerant evaporation temperature for various refrigerant mass flow rate.

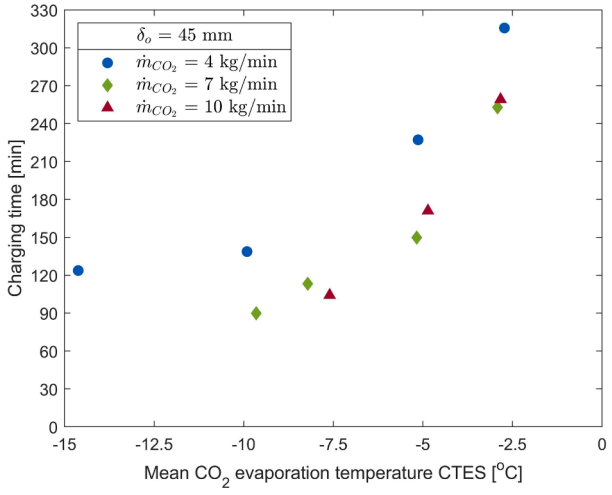

Fig. 8. Charging time for of CTES unit with plate-to-plate pitch of 45 mm as a function of the refrigerant evaporation temperature for various refrigerant mass flow rate.

increasing the refrigerant mass flow rate for the same evaporation temperature and plate pitch. Increasing the flow rate from $\dot{m}_{CO_2}$ = 4 kg/min to $\dot{m}_{CO_2}$ = 7 kg/min yields the largest reduction in charging time, while only a marginal decrease in charging time is observed when further increasing the flow rate to $\dot{m}_{CO_2}$ = 10 kg/min. This observation is explained by the insufficient refrigerant supply to the CTES unit when using the lowest flow rate, as described in detail above. Using a flow rate of $\dot{m}_{CO_2}$ = 7 kg/min provides sufficient refrigerant for the charging process and increasing to a higher mass flow rate does not provide any further benefits. In fact, a higher refrigerant mass flow rate is associated with higher pressure drop through the CTES unit (see Fig. 4. Therefore a refrigerant mass flow rate of $\dot{m}_{CO_2}$ = 7 kg/min is recommended to operate the charging process. Comparing the charging time between the three plate pitches (Figs. 6–8) for the same evaporation temperature level and mass flow rate, it is clear that the shortest charging time is recorded for the smallest plate pitch (δ_o = 15 mm). This result is expected because increasing the plate pitch increases the amount of storage medium between every PP. Consequently, more energy needs to be stored to complete the charging cycle. For an evaporation temperature of about −8.5 °C and mass flow rate of 7 kg/min, the charging time increases by 87% and 297% when increasing the plate pitch from 15 mm to 30 mm and 45 mm, respectively. For a pitch of 30 mm (Fig. 7), an additional CO_2 evaporation temperature level of approximately −1.7 °C was tested for all three refrigerant mass flow rates. It was found that the charging time has increased by 95% compared to an evaporation temperature of −2.7 °C for a refrigerant mass flow rate of 7 kg/min. Since increasing the evaporation temperature by 1 K resulted in almost double the charging time, this evaporation temperature level was excluded for the 15 mm and 30 mm configurations. Therefore, the recommended upper limit for the evaporation temperature during the charging process is −2.5 °C when implementing the CTES unit into a refrigeration system.

Table 3 shows the approximate active volume of the storage medium and the calculated maximum theoretical latent storage capacity of the CTES unit for the three configurations using Eq. 2. The density of ice is 916.74 kg/m^3, and the enthalpy of fusion is 333.43 kJ/kg [62]. Furthermore, the charging time for each configuration for a refrigerant evaporation temperature of −5 °C and mass flow rate of 7 kg/min is indicated as a reference. Increasing the plate-to-plate pitch from 15 mm to 30 mm yielded an increase of about 116% in latent storage capacity and the charging time by about 142%. By increasing the plate-to-plate pitch from 15 mm to 45 mm, the theoretical latent storage capacity increased by about 233% and the charging time increased by about 347%.

5.2. Discharging cycle

This section presents the results obtained from the discharging tests described in Section 3.2. The discharging rate for tests using a refrigerant mass flow rate of 7 kg/min and a condensing temperature varying from 5 °C to 10 °C for a PP pitch of 15 mm, 30 mm, and 45 mm are presented in Fig. 9a, b, and c, respectively. One may clearly note that the discharging cycles start with a high discharge rate (18–16 kW) for the first 20–35 min due to adjacency of ice to the PP surface and a high temperature difference between the refrigerant inside the PPs and the storage medium (initial temperature about −5 °C). However, the discharge rate is limited during this initial phase by the maximum installed heating capacity of the electric heaters in the glycol system that provides the heat load to the refrigerant (18 kW, see Section 2.2). This initial phase of high discharge rate is the longest for the highest CO_2 condensing temperature. This period constitutes a higher fraction of the total discharging time for the shortest plate pitch (15 mm) due to the melting of a significant share of the ice block. As the discharging process progresses, the discharging rates decrease towards zero, denoting the end of the process. From the ice melting process point of view, a large amount of heat (16–18 kW) is absorbed by the ice block formed between the plates, the ice melts, and thin liquid layers are formed from both sides of the PP. As the discharging process advances, the liquid layers become thicker while the ice block becomes thinner. This water layer between the ice block and the PP surface constitutes a thermal resistance to the heat transfer process, and the growth of the liquid layer results in a decrease in the discharge rate. Furthermore, the highest mean discharging rates of 7.97 kW (δ_o = 15 mm), 9.82 kW (δ_o = 30 mm) and 7.90 kW (δ_o = 45 mm) are achieved using the highest refrigerant condensing temperatures for each plate pitch (7.9 °C, 8.5 °C and 9.0 °C), due to the larger difference between the refrigerant inlet temperature and the storage medium. For the 15 mm configuration (Fig. 9a) the discharging

Table 3
Calculated maximum theoretical latent storage capacity of the CTES unit in various configurations. Charging time is given for a refrigerant mass flow rate of 7 kg/min and a evaporation temperature of −5 °C.

δ_o [mm]	$\delta_{o,mean}$ [mm]	$V_{PCM,tot}$ [m^3]	$E_{lat,th}$ [kWh]	t_C [min]
15	12.85	0.1271	10.80	34
30	27.85	0.2755	23.40	81
45	42.85	0.4240	36.00	150

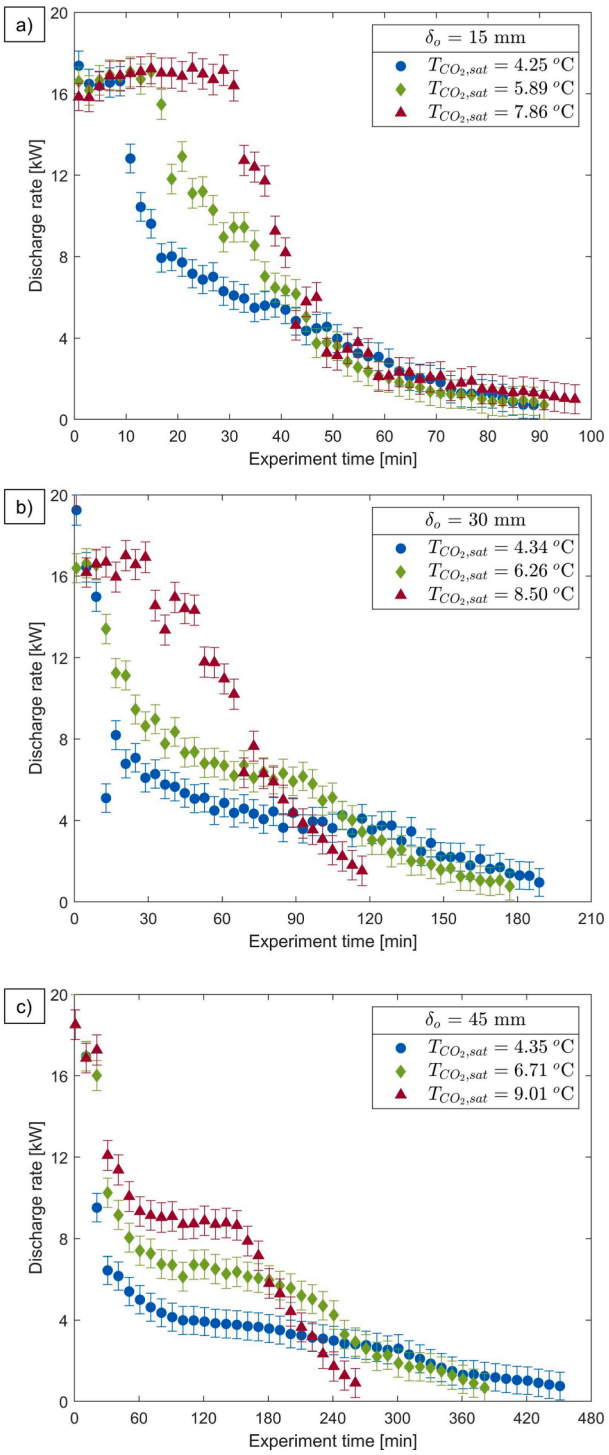

Fig. 9. Discharging rate of the CTES unit over the discharging cycle using a refrigerant mass flow rate of 7 kg/min for various refrigerant condensation temperatures for plate-to-plate pitch of a) 15 mm b) 30 mm c) 45 mm.

time is similar for the three condensing temperatures (4.25 °C, 5.89 °C and 7.86 °C). In contrast, the discharging time using a pitch of 30 mm (Fig. 9b) and 45 mm (Fig. 9c) is significantly shorter for the highest condensing temperature (8.50 °C and 9.01 °C, respectively) compared to the middle and low condensing temperatures. The most significant difference in the discharging time when varying T_{CO_2} is observed for the largest plate-to-plate pitch (δ_o = 45 mm).

The mean discharge rate and discharged energy over the discharging cycle as a function of the refrigerant mass flow rate when using a condensation temperature of 6 °C is presented in Fig. 10 and 11, respectively. From Fig. 10 the general observation is that increasing the refrigerant mass flow rate increases the mean discharge rate for all plate pitches. The one exception is for the 15 mm configuration, where 4 kg/min and 7 kg/min show similar discharge rates. For the 30 mm configuration, the mean discharge rate increases by 21.6% and 58.2% when increasing the refrigerant mass flow rate from 4 kg/min to 7 kg/min and 10 kg/min, respectively. Furthermore, the mean discharge rate decreases when increasing the plate-to-plate pitch. For a refrigerant mass flow rate of 10 kg/min, the mean discharge rate is reduced by 17.8% and 36.5% when increasing the plate pitch from 15 mm to 30 mm and 45 mm, respectively. From Fig. 11 it can be observed that the discharged energy over the cycle is increasing when increasing the plate-to-plate pitch. The higher amount of discharged energy is due to a thicker ice block between each plate that gives more thermal energy stored in the PP-HEX. Furthermore, a mass flow rate of 7 kg/min results in the highest amount of discharged energy over the cycle for all three plate pitches. The difference in discharged energy by varying the mass flow rate is most pronounced for the largest plate pitch with a difference in stored energy of 8.2%, 18.8% and 23.0% for the 15 mm, 30 mm and 45 mm configuration, respectively.

Table 4 give a summary and comparison of the discharging performance of the CTES unit for the three plate-to-plate configurations for a refrigerant mass flow rate of 7 kg/min. For the 30 mm and 45 mm plate-to-plate pitch, the discharging time is significantly reduced by increasing the condensing temperature of the refrigerant. On the other hand, the condensing temperature has no considerable effect on the discharging time for the 15 mm HEX configuration. Consequently, the thermal energy of the CTES unit is discharged over a shorter period. As discussed before, a larger temperature difference between the condensing refrigerant and the storage medium increases the driving force for the heat transfer process during the discharging cycle. This effect is particularly important for the larger plate-to-plate pitches (30 mm and 45 mm) because of the increased thermal resistance caused by the thicker liquid layer forming on the PP surface compared to the 15 mm plate pitch. Table 4 includes the ratio of total discharged energy to the maximum theoretical latent storage capacity. It can be observed that the discharged energy is lower than the theoretical maximum capacity of the unit, except for the highest condensing temperature using a pitch of 15 mm. For the total discharge energy measured in the experiments (E_D), the contribution from both the latent heat storage and sensible heat storage in the CTES is included. Since the theoretical maximum latent storage capacity ($E_{lat,th}$) includes only the latent heat storage, the ratio of the total discharged energy to the maximum theoretical latent storage

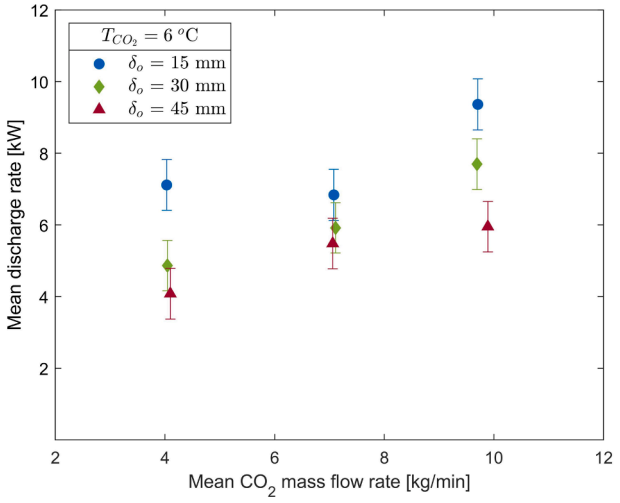

Fig. 10. Mean discharge rate as a function of refrigerant mass flow rate for a refrigerant condensation temperature of 6 °C.

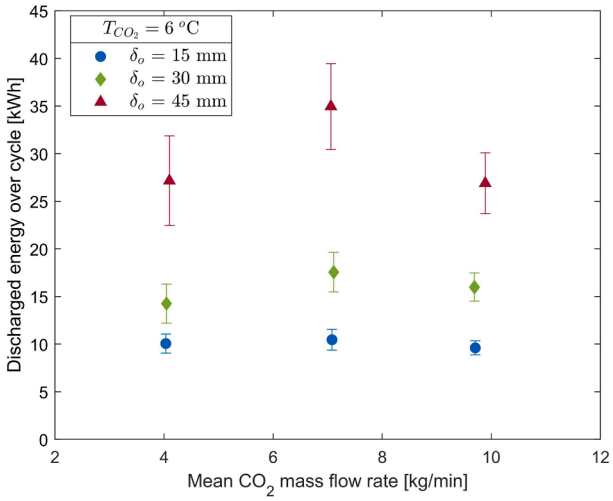

Fig. 11. Discharged energy as a function of refrigerant mass flow rate for a refrigerant condensation temperature of 6 °C.

Table 4
Summary of the discharging performance employing a refrigerant mass flow rate of $\dot{m}_{CO_2} = 7$ kg/min for various plate-to-plate configurations.

δ_o [mm]	T_c [°C]	$\dot{E}_r$ [kW]	E_D [kWh]	$E_D/E_{lat,th}$	t_D [min]
15	4.26	5.82 ± 0.687	8.62 ± 1.02	0.799	89
15	5.89	6.84 ± 0.712	10.46 ± 1.09	0.969	92
15	7.86	7.97 ± 0.725	12.91 ± 1.17	1.20	97
30	4.34	4.67 ± 0.690	14.76 ± 2.18	0.680	190
30	6.26	5.92 ± 0.702	17.56 ± 2.09	0.809	178
30	8.50	9.82 ± 0.732	19.69 ± 1.47	0.907	121
45	4.35	3.55 ± 0.687	26.90 ± 5.21	0.747	455
45	6.71	5.48 ± 0.705	34.95 ± 4.50	0.971	383
45	9.01	7.90 ± 0.725	35.29 ± 3.24	0.980	268

capacity can be larger than one. It can also be observed that the 15 mm configuration had the highest ratio of discharged energy to theoretical storage capacity for all refrigerant condensing temperatures due to the proximity of the ice block to the PP over the whole cycle. There are multiple explanations why the ratio of the discharged energy to the theoretical storage capacity generally is lower than one. Indeed, when calculating the theoretical latent storage capacity, the entire surface of the PP is assumed to be covered by solid ice. When the charging tests are completed, no ice around the outer edges of the PP was completely formed. This edge effect will be less critical for a full-size CTES unit using larger PP sizes than in the present study. Moreover, at the locations where the refrigerant turns around the longitudinal seam welds to start the next flow pass, the ice did not form at the outer edge (see Fig. 3). This effect was most visible for the lowest refrigerant mass flow rate, indicating a poor refrigerant distribution in this section of the PP. Possible solutions to this issue are to increase the length of the longitudinal seam welds or manufacture the PP with more refrigerant flow passes. The latter will improve the refrigerant distribution by creating narrower channels and a longer flow length for the refrigerant at the cost of increasing the pressure loss. Overall, it can be concluded that a refrigerant flow rate of 7 kg/min is convenient to ensure adequate refrigerant distribution for the current design of the PP. However, the refrigerant distribution can be improved by including more flow passes for the refrigerant for future work.

Table 4 can be used as a design guide for the practical implementation of this type of CTES unit into a refrigeration plant. Given that peak shaving of the refrigeration demand is the aim of the CTES implementation, the designer must have an accurate prediction of the load curve of the refrigeration plant. Based on the desired peak reduction and peak duration, the adequate CTES configuration and operating conditions can be selected based on Table 4. As a general recommendation, the 15 mm configuration will be a good fit for reducing a peak with a short duration (1–1.5 h) and a relatively high refrigeration load. To achieve peak shaving for a peak with a lower magnitude and a duration in the range of 4 to 6 h, the 45 mm configuration is the appropriate selection. If more storage capacity or a higher discharge rate is required than provided by a single CTES unit, two or more units can be installed in parallel. Furthermore, this CTES unit can also be installed as a subcooler in a similar configuration as presented by Korth et al. [32]. Using a thermal energy storage unit as a subcooler has been proven to effectively increase the COP of the refrigeration cycles by increasing the evaporation capacity or by reducing the throttling losses in the case of CO_2 systems [11].

6. Conclusions

This paper presents the development of a novel Cold Thermal Energy Storage (CTES) unit and the associated experimental test facility. Inside the CTES unit, the Heat Exchanger (HEX) employs Pillow Plates (PP) to exchange heat between the latent storage medium (ice/water) and the refrigerant (CO_2). It is designed to be integrated directly into the primary refrigerant circuit to achieve peak shaving of the refrigeration demand. This work is one of the very few experimental demonstrations of a CTES unit that couples the isothermal phase change process of the latent storage medium with the isothermal phase change process of the refrigerant. The work provides important knowledge on the performance of latent CTES units in refrigeration systems. The main results from the experimental characterisation are summarised as follows:

- The main parameter affecting the charging time of the CTES unit was found to be the refrigerant evaporation temperature. Reducing the charging temperature is associated with an increase in the energy consumption of the refrigeration system due to increased pressure lift of the compressor. For the 15 and 30 mm HEX configurations, a refrigerant evaporation temperature of −5 °C is a suitable option. A more linear dependency between the charging time and the evaporation temperature was observed for the 45 mm plate-to-plate pitch. The evaporation temperature should be selected based on the time available for charging in the system where the unit is installed. A refrigerant mass flow rate of 7 kg/min resulted in an adequate refrigerant distribution within the ten PP in the plate stack, ensuring flooded operation during the whole charging process.
- The discharging rate of the CTES unit was highly transient during the discharging process, yielding a high discharge rate during the initial phase that continuously decreases towards the end. The refrigerant condensing temperature is the main parameter affecting the mean discharge rate of the discharging process. The highest amount of energy discharged for the 45 mm configuration was 35.29 kWh in approximately 4.5 h, with a mean discharge rate of 7.90 kW.
- The flexible construction of the PP-HEX inside the CTES unit enables the designer to match the discharging rate and storage capacity of the CTES unit to the refrigeration load curve of the system to be considered. For a system with relatively short peaks with high magnitude, the 15 mm configuration is the best choice. If the load peak lasts up to 6 h and requires higher latent storage capacity, the 45 mm configuration is a suitable alternative.

Further experimental work could include an investigation of partial charging and discharging cycles of the CTES unit and the resulting consequences for the performance. A continuation of present work is ongoing with replacing the storage medium ice/water with an organic Phase Change Material (PCM) that is suitable to achieve peak shaving in refrigeration systems used in an industrial food processing plant.

Declaration of Competing Interest

The authors declare that they have no known competing financial interests or personal relationships that could have appeared to influence the work reported in this paper.

Acknowledgements

The work is part of HighEFF - Centre for an Energy Efficient and Competitive Industry for the Future, an 8-year Research Centre under the FME-scheme (Centre for Environment-friendly Energy Research, 257632). The first author gratefully acknowledges the financial support from the Research Council of Norway and user partners of HighEFF. The authors would also like to acknowledge the financial and technical support of Skala Fabrikk AS, Hermetic Pumpen GmbH, Alfa Laval, HB Products and Danfoss regarding the test facility.

References

[1] K.J. Dyke, N. Schofield, M. Barnes, The impact of transport electrification on electrical networks, IEEE Trans. Industr. Electron. 57 (2010) 3917–3926.
[2] L.P. Fernandez, T.G. San Roman, R. Cossent, C.M. Domingo, P. Frias, Assessment of the impact of plug-in electric vehicles on distribution networks, IEEE Trans. Power Syst. 26 (2010) 206–213.
[3] W. Su, H. Eichi, W. Zeng, M.-Y. Chow, A survey on the electrification of transportation in a smart grid environment, IEEE Trans. Industr. Inf. 8 (2011) 1–10.
[4] S. Lechtenböhmer, L.J. Nilsson, M. Åhman, C. Schneider, Decarbonising the energy intensive basic materials industry through electrification–implications for future eu electricity demand, Energy 115 (2016) 1623–1631.
[5] International Energy Agency, Cooling, IEA, Paris, 2020.
[6] International Energy Agency, The Future of Cooling: Opportunities for energy-efficient air conditioning, IEA Publications, 2018.
[7] I. Dincer, M. Rosen, Thermal energy storage: systems and applications, John Wiley & Sons, 2002.
[8] Y. Yau, B. Rismanchi, A review on cool thermal storage technologies and operating strategies, Renew. Sustain. Energy Rev. 16 (2012) 787–797.
[9] Y. Sun, S. Wang, F. Xiao, D. Gao, Peak load shifting control using different cold thermal energy storage facilities in commercial buildings: A review, Energy Convers. Manage. 71 (2013) 101–114.
[10] E. Oró, A. De Gracia, A. Castell, M.M. Farid, L.F. Cabeza, Review on phase change materials (pcms) for cold thermal energy storage applications, Appl. Energy 99 (2012) 513–533.
[11] H. Selvnes, Y. Allouche, R.I. Manescu, A. Hafner, Review on cold thermal energy storage applied to refrigeration systems using phase change materials, Therm. Sci. Eng. Prog. 22 (2021) 100807.
[12] A.L. Gómez, Review of Energy Efficient Technologies in the Refrigeration Systems of the Agrofood Industry, Institut Català d'Energia (1995).
[13] N. Tay, M. Belusko, F. Bruno, An effectiveness-ntu technique for characterising tube-in-tank phase change thermal energy storage systems, Appl. Energy 91 (2012) 309–319.
[14] N. Tay, M. Belusko, F. Bruno, Experimental investigation of tubes in a phase change thermal energy storage system, Appl. Energy 90 (2012) 288–297.
[15] N. Tay, F. Bruno, M. Belusko, Experimental validation of a cfd and an ε-ntu model for a large tube-in-tank pcm system, Int. J. Heat Mass Transf. 55 (2012) 5931–5940.
[16] N. Tay, F. Bruno, M. Belusko, Experimental validation of a cfd model for tubes in a phase change thermal energy storage system, Int. J. Heat Mass Transf. 55 (2012) 574–585.
[17] Y. Allouche, S. Varga, C. Bouden, A.C. Oliveira, Experimental determination of the heat transfer and cold storage characteristics of a microencapsulated phase change material in a horizontal tank, Energy Convers. Manage. 94 (2015) 275–285.
[18] A. Abhishek, B. Kumar, M.H. Kim, Y.T. Lee, J.D. Chung, S.T. Kim, T. Kim, C. Lee, K. Lee, Comparison of the performance of ice-on-coil ltes tanks with horizontal and vertical tubes, Energy Build. 183 (2019) 45–53.
[19] A. Castell, M. Belusko, F. Bruno, L.F. Cabeza, Maximisation of heat transfer in a coil in tank pcm cold storage system, Appl. Energy 88 (2011) 4120–4127.
[20] M.A. Ezan, A. Erek, I. Dincer, Energy and exergy analyses of an ice-on-coil thermal energy storage system, Energy 36 (2011) 6375–6386.
[21] A. López-Navarro, J. Biosca-Taronger, B. Torregrosa-Jaime, J. Corberán, J. Bote-García, J. Payá, Experimental investigations on the influence of ice floating in an internal melt ice-on-coil tank, Energy Build. 57 (2013) 20–25.
[22] A. López-Navarro, J. Biosca-Taronger, B. Torregrosa-Jaime, I. Martínez-Galván, J. M. Corberán, J. Esteban-Matías, J. Paya, Experimental investigation of the temperatures and performance of a commercial ice-storage tank, Int. J. Refrig. 36 (2013) 1310–1318.
[23] B. Torregrosa-Jaime, A. López-Navarro, J.M. Corberán, J. Esteban-Matías, L. Klinkner, J. Payá, Experimental analysis of a paraffin-based cold storage tank, Int. J. Refrig. 36 (2013) 1632–1640.
[24] A. López-Navarro, J. Biosca-Taronger, J. Corberán, C. Peñalosa, A. Lázaro, P. Dolado, J. Payá, Performance characterization of a pcm storage tank, Appl. Energy 119 (2014) 151–162.
[25] F. Bosholm, A. López-Navarro, M. Gamarra, J. Corberán, J. Payá, Reproducibility of solidification and melting processes in a latent heat thermal storage tank, Int. J. Refrig. 62 (2016) 85–96.
[26] R.M. Saeed, J.P. Schlegel, R. Sawafta, V. Kalra, Plate type heat exchanger for thermal energy storage and load shifting using phase change material, Energy Convers. Manage. 181 (2019) 120–132.
[27] W. Lin, W. Zhang, Z. Ling, X. Fang, Z. Zhang, Experimental study of the thermal performance of a novel plate type heat exchanger with phase change material, Appl. Therm. Eng. 178 (2020) 115630.
[28] T. Korth, F. Loistl, C. Schweigler, Novel integration of latent heat storage in multi-split air conditioning systems, in: 25th IIR International Congress of Refrigeration Proceedings, International Institute of Refrigeration, 2019.
[29] F. Wang, G. Maidment, J. Missenden, R. Tozer, The novel use of phase change materials in refrigeration plant. part 1: Experimental investigation, Appl. Therm. Eng. 27 (2007) 2893–2901.
[30] F. Wang, G. Maidment, J. Missenden, R. Tozer, The novel use of phase change materials in refrigeration plant. part 2: Dynamic simulation model for the combined system, Appl. Therm. Eng. 27 (2007) 2902–2910.
[31] F. Wang, G. Maidment, J. Missenden, R. Tozer, The novel use of phase change materials in refrigeration plant. part 3: Pcm for control and energy savings, Appl. Therm. Eng. 27 (2007) 2911–2918.
[32] T. Korth, F. Loistl, A. Storch, R. Schex, A. Krönauer, C. Schweigler, Capacity enhancement of air conditioning systems by direct integration of a latent heat storage unit, Appl. Therm. Eng. 167 (2020) 114727.
[33] Sasol Chemicals, Parafol 16-97, 2020. URL: https://products.sasol.com/pic/products/home/grades/AS/5parafol-16-97/index.html/.
[34] J. Mitrovic, R. Peterson, Vapor condensation heat transfer in a thermoplate heat exchanger, Chem. Eng. Technol. Ind. Chem. Plant Equip. Process Eng. Biotechnol. 30 (2007) 907–919.
[35] J. Tran, S. Sommerfeld, M. Piper, E. Kenig, Investigation of pillow-plate condensers for the application in distillation columns, Chem. Eng. Res. Des. 99 (2015) 67–74.
[36] J. Tran, M. Linnemann, M. Piper, E. Kenig, On the coupled condensation-evaporation in pillow-plate condensers: Investigation of cooling medium evaporation, Appl. Therm. Eng. 124 (2017) 1471–1480.
[37] J. Mitrovic, B. Maletic, Numerical simulation of fluid flow and heat transfer in thermoplates, Chem. Eng. Technol. 34 (2011) 1439–1448.
[38] M. Piper, A. Zibart, J. Tran, E. Kenig, Numerical investigation of turbulent forced convection heat transfer in pillow plates, Int. J. Heat Mass Transf. 94 (2016) 516–527.
[39] M. Piper, A. Zibart, E. Kenig, New design equations for turbulent forced convection heat transfer and pressure loss in pillow-plate channels, Int. J. Therm. Sci. 120 (2017) 459–468.
[40] O. Arsenyeva, J. Tran, M. Piper, E. Kenig, An approach for pillow plate heat exchangers design for single-phase applications, Appl. Therm. Eng. 147 (2019) 579–591.
[41] M. Shirzad, M.A. Delavar, S.S.M. Ajarostaghi, K. Sedighi, Evaluation the effects of geometrical parameters on the performance of pillow plate heat exchanger, Chem. Eng. Res. Des. 150 (2019) 74–83.
[42] S. Kumar, B. Premachandran, P. Subbarao, Study on thermo–hydraulics in a pillow plate channel, Int. J. Therm. Sci. 145 (2019) 106020.
[43] M. Piper, A. Olenberg, J. Tran, E. Kenig, Determination of the geometric design parameters of pillow-plate heat exchangers, Appl. Therm. Eng. 91 (2015) 1168–1175.
[44] G. Lorentzen, The use of natural refrigerants: a complete solution to the cfc/hcfc predicament, Int. J. Refrig. 18 (1995) 190–197.
[45] R. Ciconkov, Refrigerants: There is still no vision for sustainable solutions, Int. J. Refrig. 86 (2018) 441–448.
[46] P. Gullo, A. Hafner, K. Banasiak, Transcritical r744 refrigeration systems for supermarket applications: Current status and future perspectives, Int. J. Refrig. 93 (2018) 269–310.
[47] K.Z. Skačanová, M. Battesti, Global market and policy trends for co2 in refrigeration, Int. J. Refrig. 107 (2019) 98–104.
[48] P. Nekså, H. Rekstad, G.R. Zakeri, P.A. Schiefloe, Co2-heat pump water heater: characteristics, system design and experimental results, Int. J. Refrig. 21 (1998) 172–179.
[49] J. Rogstam, Evolution of co2 as refrigerant in ice rink applications, in: 12th IIR Gustav Lorentzen Natural Working Fluids Conference, Edinburgh, UK, Aug 2016, pp. 21–24.
[50] H. Selvnes, A. Hafner, H. Kauko, Design of a cold thermal energy storage unit for industrial applications using co2 as refrigerant, in: 25th IIR International Congress of Refrigeration Proceedings, IIR, 2019.
[51] H. Selvnes, V. Büttner, A. Hafner, Evaluation of a pillow-plate heat exchanger for a pump-circulated CO2 refrigeration system, in: Proceedings of the 14th IIR-Gustav Lorentzen Conference on Natural Refrigerants, International Institute of Refrigeration, 2020.
[52] C. Elliott, V. Vijayakumar, W. Zink, R. Hansen, National instruments labview: a programming environment for laboratory automation and measurement, JALA, J. Assoc. Lab. Autom. 12 (2007) 17–24.
[53] Refrigera Industriale, Refrigera 2-way ball valves, 2015. URL: https://www.refrigera.eu/en/ball-valves/2-way-ball-valve.
[54] HERMETIC Pumpen GmbH, HERMETIC refrigeration pumps, 2021. URL: https://kaelte.hermetic-pumpen.com/en/pump-types.

[55] DOW Chemical Company, DOWCAL 200 Heat Transfer Fluid Technical Data Sheet, 2021. URL: https://www.dow.com/en-us/document-viewer.html?ramdomVar=2372344082032526391&docPath=/content/dam/dcc/documents/en-us/productdatasheet/180/180-01589-01-dowcal-200-heat-transfer-fluid-tds.pdf.
[56] I. ISO, B. OIML, Guide to the expression of uncertainty in measurement, Geneva, Switzerland 122 (1995) 16–17.
[57] E. Lemmon, I. Bell, M. Huberm, M. McLinden, NIST Standard Reference Database 23: Reference Fluid Thermodynamic and Transport Properties-REFPROP, Version 10.0, National Institute of Standards and Technology, 2018. URL: https://www.nist.gov/srd/refprop.
[58] S. Minetto, R. Brignoli, C. Zilio, S. Marinetti, Experimental analysis of a new method for overfeeding multiple evaporators in refrigeration systems, Int. J. Refrig. 38 (2014) 1–9.
[59] S. Bortolin, M. Rossato, S. Bernardinello, D. Del Col, Investigation of evaporator performance with and without liquid overfeeding (2016).
[60] G. Mitsopoulos, E. Syngounas, D. Tsimpoukis, E. Bellos, C. Tzivanidis, S. Anagnostatos, Annual performance of a supermarket refrigeration system using different configurations with co2 refrigerant, Energy Convers. Manage. X 1 (2019) 100006.
[61] A. Tambovtsev, H. Quack, Cop improvement by transfer of the superheating into the internal heat exchanger, in: International Congress of Refrigeration, Beijing, China, 2007.
[62] R. Feistel, W. Wagner, A new equation of state for h 2 o ice ih, J. Phys. Chem. Ref. Data 35 (2006) 1021–1047.